Machine Learning-based Prognostic Modeling using Clinical Data and Quantitative Radiomic Features from Chest CT Images in COVID-19 Patients

Shiri Lord, Isaac; Sorouri, Majid; Geramifar, Parham; Nazari, Mostafa; Abdollahi, Mohammad; Salimi, Yazdan; Khosravi, Bardia; Askari, Dariush; Aghaghazvini, Leila; Hajianfar, Ghasem; Kasaeian, Amir; Abdollahi, Hamid; Arabi, Hossein; Rahmim, Arman [**and 2 more**]

How to cite

SHIRI LORD, Isaac et al. Machine Learning-based Prognostic Modeling using Clinical Data and Quantitative Radiomic Features from Chest CT Images in COVID-19 Patients. In: Computers in Biology and Medicine, 2021, vol. 132, p. 104304. doi: 10.1016/j.compbiomed.2021.104304

This publication URL: https://archive-ouverte.unige.ch/unige:151811

Publication DOI: 10.1016/j.compbiomed.2021.104304

Computers in Biology and Medicine 132 (2021) 104304

Contents lists available at ScienceDirect

Computers in Biology and Medicine

journal homepage: http://www.elsevier.com/locate/compbiomed

Machine learning-based prognostic modeling using clinical data and quantitative radiomic features from chest CT images in COVID-19 patients

Isaac Shiri [a,1], Majid Sorouri [b,1], Parham Geramifar [c], Mostafa Nazari [d], Mohammad Abdollahi [b], Yazdan Salimi [a], Bardia Khosravi [b], Dariush Askari [e], Leila Aghaghazvini [f], Ghasem Hajianfar [g], Amir Kasaeian [b,h,i], Hamid Abdollahi [j], Hossein Arabi [a], Arman Rahmim [k,l], Amir Reza Radmard [f,**], Habib Zaidi [a,m,n,o,*]

[a] *Division of Nuclear Medicine and Molecular Imaging, Geneva University Hospital, CH-1211, Geneva, Switzerland*
[b] *Digestive Diseases Research Center, Digestive Diseases Research Institute, Tehran University of Medical Sciences, Tehran, Iran*
[c] *Research Center for Nuclear Medicine, Shariati Hospital, Tehran University of Medical Sciences, Tehran, Iran*
[d] *Department of Biomedical Engineering and Medical Physics, Shahid Beheshti University of Medical Sciences, Tehran, Iran*
[e] *Department of Radiology Technology, Shahid Beheshti University of Medical Sciences, Tehran, Iran*
[f] *Department of Radiology, Shariati Hospital, Tehran University of Medical Sciences, Tehran, Iran*
[g] *Rajaie Cardiovascular Medical and Research Center, Iran University of Medical Sciences, Tehran, Iran*
[h] *Hematology, Oncology and Stem Cell Transplantation Research Center, Research Institute for Oncology, Hematology and Cell Therapy, Tehran University of Medical Sciences, Tehran, Iran*
[i] *Inflammation Research Center, Tehran University of Medical Sciences, Tehran, Iran*
[j] *Department of Radiologic Sciences and Medical Physics, Kerman University of Medical Sciences, Kerman, Iran*
[k] *Departments of Radiology and Physics, University of British Columbia, Vancouver, BC, Canada*
[l] *Department of Integrative Oncology, BC Cancer Research Institute, Vancouver, BC, Canada*
[m] *Geneva University Neurocenter, Geneva University, Geneva, Switzerland*
[n] *Department of Nuclear Medicine and Molecular Imaging, University of Groningen, University Medical Center Groningen, Groningen, Netherlands*
[o] *Department of Nuclear Medicine, University of Southern Denmark, Odense, Denmark*

ARTICLE INFO

Keywords:
COVID-19
Computed tomography (CT)
Radiomics
Prognosis
Modeling

ABSTRACT

Objective: To develop prognostic models for survival (alive or deceased status) prediction of COVID-19 patients using clinical data (demographics and history, laboratory tests, visual scoring by radiologists) and lung/lesion radiomic features extracted from chest CT images.

Methods: Overall, 152 patients were enrolled in this study protocol. These were divided into 106 training/validation and 46 test datasets (untouched during training), respectively. Radiomic features were extracted from the segmented lungs and infectious lesions separately from chest CT images. Clinical data, including patients' history and demographics, laboratory tests and radiological scores were also collected. Univariate analysis was first performed (q-value reported after false discovery rate (FDR) correction) to determine the most predictive features among all imaging and clinical data. Prognostic modeling of survival was performed using radiomic features and clinical data, separately or in combination. Maximum relevance minimum redundancy (MRMR) and XGBoost were used for feature selection and classification. The receiver operating characteristic (ROC) curve and the area under the ROC curve (AUC), sensitivity, specificity, and accuracy were used to assess the prognostic performance of the models on the test datasets.

Results: For clinical data, cancer comorbidity (q-value < 0.01), consciousness level (q-value < 0.05) and radiological score involved zone (q-value < 0.02) were found to have high correlated features with outcome. Oxygen saturation (AUC $= 0.73$, q-value < 0.01) and Blood Urea Nitrogen (AUC $= 0.72$, q-value $= 0.72$) were identified as high clinical features. For lung radiomic features, SAHGLE (AUC $= 0.70$) and HGLZE (AUC $= 0.67$) from GLSZM were identified as most prognostic features. Amongst lesion radiomic features, RLNU from GLRLM (AUC $= 0.73$), HGLZE from GLSZM (AUC $= 0.73$) had the highest performance. In multivariate analysis,

---

* Corresponding author. Geneva University Hospital, Division of Nuclear Medicine and Molecular Imaging, CH-1211, Geneva, Switzerland.

** Corresponding author. Department of Radiology, Shariati Hospital, Tehran University of Medical Sciences, Tehran, Iran.

E-mail addresses: radmard@tums.ac.ir (A.R. Radmard), habib.zaidi@hcuge.ch (H. Zaidi).

[1] Both authors contributed equally to this manuscript.

https://doi.org/10.1016/j.compbiomed.2021.104304
Received 8 January 2021; Received in revised form 26 February 2021; Accepted 27 February 2021

combining lung, lesion and clini
(AUC = 0.95 ± 0.029 (95%CI: 0.
0.066 (95% CI = 0.87–0.9) and s
Conclusion: Combination of radic
patients. The developed model ha

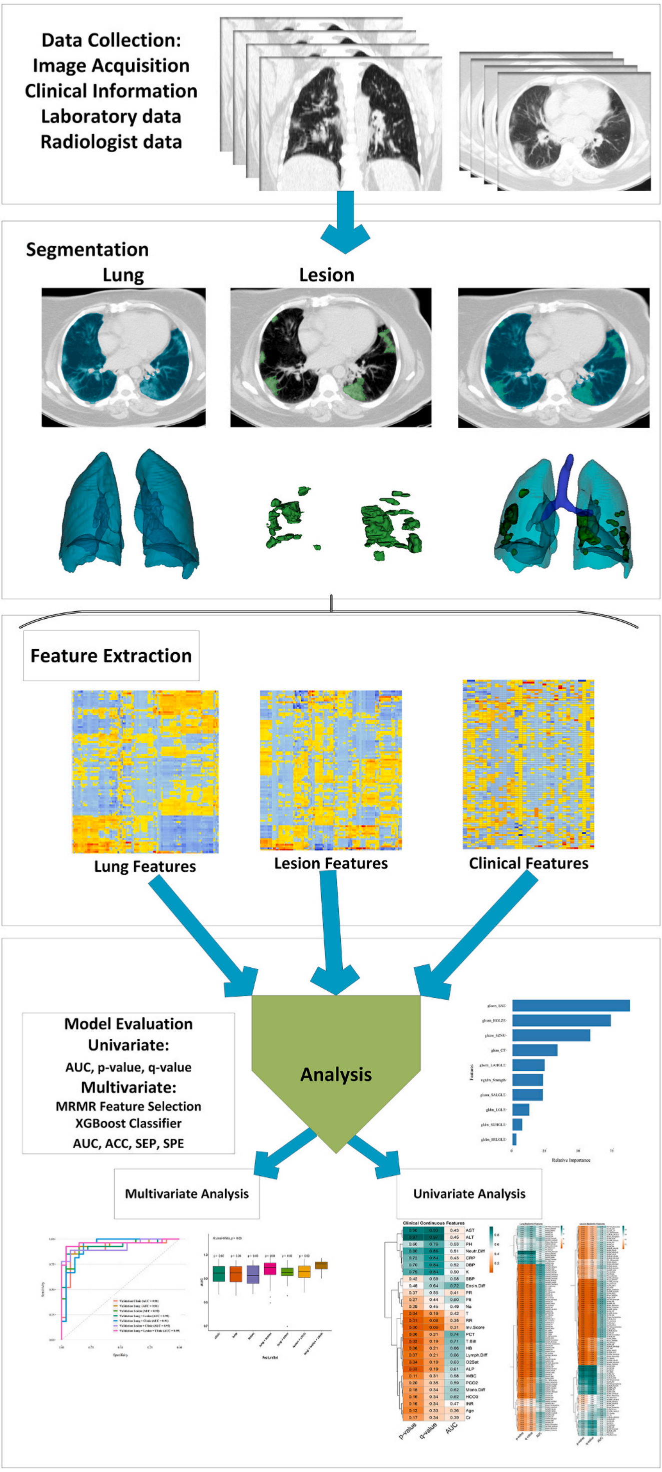

Fig. 1. Flowchart of the adopted study protocol.

1. Introduction

Severe acute respiratory syndrome coronavirus 2 (SARS-CoV-2) disease (COVID-19) has significantly impacted global health and continues to be a major global concern as the number of infected patients and mortality are still rapidly growing [1,2]. The first line approach to diagnose COVID-19 involves the usage of a molecular diagnostic method, referred to as real-time quantitative reverse transcription-polymerase chain reaction (qPCR) assay [3]. In addition, X-ray computed tomography (CT) has garnered much clinical and research interest for the management of COVID-19 patients [4]. Several studies have compared the two diagnostic methods and documented their benefits and limitations. For instance, some of these studies reported that qPCR has variable sensitivity for different biological samples, while CT was unable to detect small infected lung regions [3–5]. Furthermore, the importance of predicting patients' prognosis based on early findings in the course of the disease has been an area of active research [6,7].

The emerging field of radiomics provides a reliable, non-invasive and cost-effective approach to improve diagnosis, prognosis and therapy response prediction in a number of diseases [8–15]. Radiomics is an image data mining framework enabling to extract extensive information from medical images using a wide range of features, based on which a correlation is established with clinical and biological findings [8,9,16–22]. Furthermore, radiomic studies can be used to provide differential diagnosis [23]. CT image radiomics are increasingly utilized for this purpose. Yanling et al. [24] developed a radiomics nomogram incorporating CT radiomic signatures and laboratory data for differentiating bacterial pneumonia from acute paraquat lung injury. In another study, Wang et al. [25] applied CT radiomics for differential diagnosis of progressive pulmonary tuberculosis from community-acquired pneumonia. Their radiomics model outperformed senior radiologists' clinical judgment [25].

A number of studies applied deep or machine learning algorithms for COVID-19 outbreak prediction, detection/segmentation of infected pneumonia regions from radiologic images, as well as new drug development and disease screening [26–35]. In diagnostic studies, artificial intelligence approaches have been applied to various medical imaging modalities, including radiography, ultrasound, and CT to build more accurate detection/diagnostic models [36,37]. For the specific case of CT, a number of radiomic studies have been conducted for detection, including screening patients from other lung infections, and prediction of hospital stay. In these studies, CT radiomic features and machine learning algorithms were used to develop and implement such models. Qi et al. [4] studied 52 COVID-19 patients for predicting hospital stay. CT radiomic features and machine learning algorithms, including logistic regression and Random Forest were employed, wherein the model exhibited area under the receiver operating characteristic (ROC) curve (AUC) values of 0.97 and 0.92 for logistic regression and Random Forest algorithms, respectively. The detection radiomic models developed by Guiot et al. [38] depicted a sensitivity and specificity of 78.9% and 91.1%, respectively, whereas the radiomics signature to detect COVID-19 from CT images developed by Fang et al. [39] achieved AUC of 0.82 for the test sets.

When utilizing radiomics and machine learning or deep learning approaches, studies have indicated that these approaches alone or in combination with clinical information have the potential to serve as substitutes for diagnosis, prognosis and therapy response performance evaluation [9,11]. In the present study, we aimed to develop prognostic models to predict survival (alive or deceased status) in COVID-19 patients. Specifically, we aimed to develop various prognostic models using CT radiomic features, clinical data (demographics and history, and laboratory tests) and radiological scores obtained from radiologist's reports.

2. Materials and methods

Fig. 1 summarizes the various steps involved in the study design.

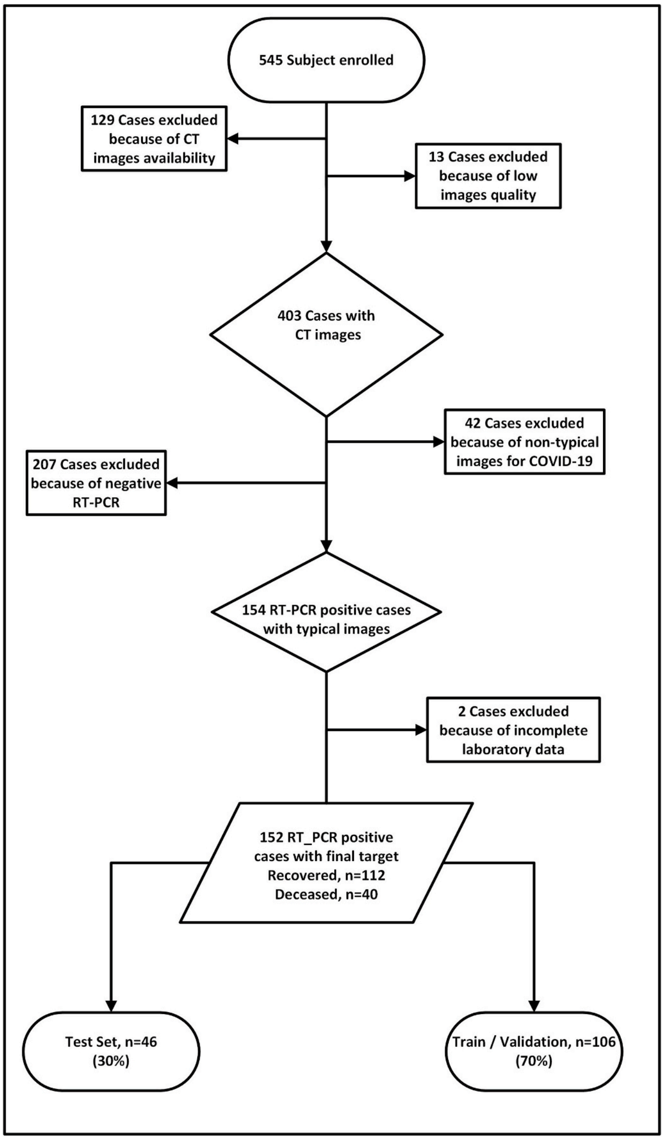

Fig. 2. Inclusion and exclusion criteria followed in the study protocol.

Transparent Reporting of a multivariable prediction model for Individual Prognosis Or Diagnosis (TRIPOD) [40] check list was reported in supplemental Table 1.

2.1. Patient population

This retrospective study was conducted with institutional review board approval. Formal written consent was waived owing to the nature of the study. All patients admitted to our tertiary center between February 11, 2020 and Jun 20, 2020 were enrolled in our study protocol. First, we collected a COVID-19 dataset by applying a set of inclusion and exclusion criteria. Our inclusion criteria were as follows: 1) patients undergoing high quality CT scans, 2) confirmation of COVID-19 by qPCR, 3) visible infected regions in the lungs, and 4) availability of clinical and radiological data and reports. The inclusion and exclusion criteria of patients are presented in Fig. 2. All patients had a median of 6 days interval between symptoms start date and admission to the hospital. All patients received one of the two standard treatment regimens administered in the hospital: Hydroxychloroquine, Lopinavir/Ritonavir. All clinical, laboratory and imaging features were extracted at the first day of admission.

Table 1
Detailed description of the extracted radiomic features used in this study protocol.

Shape Features	Gray Level Size Zone Matrix (GLSZM)	Gray Level Dependence Matrix (GLDM)
Voxel Volume (VVolume)	Small Area Emphasis (SAE)	Small Dependence Emphasis (SDE)
Mesh Volume (MVolume)	Large Area Emphasis (LAE)	Large Dependence Emphasis (LDE)
Surface Area	Gray Level Non-Uniformity (GLN)	Gray Level Non-Uniformity (GLN)
Surface Area to Volume ratio (SVR)	Gray Level Non-Uniformity Normalized (GLNN)	Dependence Non-Uniformity (DN)
Sphericity	Size-Zone Non-Uniformity (SZN)	Dependence Non-Uniformity Normalized (DNN)
Maximum 3D diameter (M3DD)	Size-Zone Non-Uniformity Normalized (SZNN)	Gray Level Variance (GLV)
Maximum 2D diameter (Slice) (M2DDS)	Zone Percentage (ZP)	Dependence Variance (DV)
Maximum 2D diameter (Column) (M2DDC)	Gray Level Variance (GLV)	Dependence Entropy (DE)
Maximum 2D diameter (Row) (M2DDR)	Zone Variance (ZV)	Low Gray Level Emphasis (LGLE)
Major Axis	Zone Entropy (ZE)	High Gray Level Emphasis (HGLE)
Minor Axis	Low Gray Level Zone Emphasis (LGLZE)	Small Dependence Low Gray Level Emphasis (SDLGLE)
Least Axis	High Gray Level Zone Emphasis (HGLZE)	Small Dependence High Gray Level Emphasis (SDHGLE)
Elongation	Small Area Low Gray Level Emphasis (SALGLE)	Large Dependence Low Gray Level Emphasis (LDLGLE)
Flatness	Small Area High Gray Level Emphasis (SAHGLE)	Large Dependence High Gray Level Emphasis (LDHGLE)
	Large Area Low Gray Level Emphasis (LALGLE)	
	Large Area High Gray Level Emphasis (LAHGLE)	
First Order Statistics (FO)	**Gray Level Co-occurrence Matrix (GLCM)**	**Gray Level Run Length Matrix (GLRLM)**
Energy	Autocorrelation (AC)	Short Run Emphasis (SRE)
Total Energy (TE)	Joint Average (JA)	Long Run Emphasis (LRE)
Entropy	Cluster Prominence (CP)	Gray Level Non-Uniformity (GLN)
Minimum	Cluster Shade (CS)	Gray Level Non-Uniformity Normalized (GLNN)
10th percentile	Cluster Tendency (CT)	Run Length Non-Uniformity (RLN)
90th percentile	Contrast	Run Length Non-Uniformity Normalized (RLNN)
Maximum	Correlation	Run Percentage (RP)
Mean	Difference Average (DA)	Gray Level Variance (GLV)
Median	Difference Entropy (DE)	Run Variance (RV)
Interquartile Range (IQR)	Difference Variance (DV)	Run Entropy (RE)
Range	Joint Energy (JEnergy)	Low Gray Level Run Emphasis (LGLRE)
Mean Absolute Deviation (MAD)	Joint Entropy (JEntropy)	High Gray Level Run Emphasis (HGLRE)
Robust Mean Absolute Deviation (RMAD)	Informal Measure of Correlation (IMC) 1	Short Run Low Gray Level Emphasis (SRLGLE)
Root Mean Squared (RMS)	Informal Measure of Correlation (IMC) 2	Short Run High Gray Level Emphasis (SRHGLE)
Skewness	Inverse Difference Moment (IDM)	Long Run Low Gray Level Emphasis (LRLGLE)
Kurtosis	Inverse Difference Moment Normalized (IDMN)	Long Run High Gray Level Emphasis (LRHGLE)
Variance	Inverse Difference (ID)	**Neighboring Gray Tone Difference Matrix (NGTDM)**
Uniformity	Inverse Difference Normalized (IDN)	Coarseness
	Inverse Variance (IV)	Contrast
	Maximum Probability (MP)	Busyness
	Maximum Correlation Coefficient (MCC)	Complexity
	Sum Average (SA)	Strength
	Sum Entropy (SE)	
	Sum of Squares (SS)	

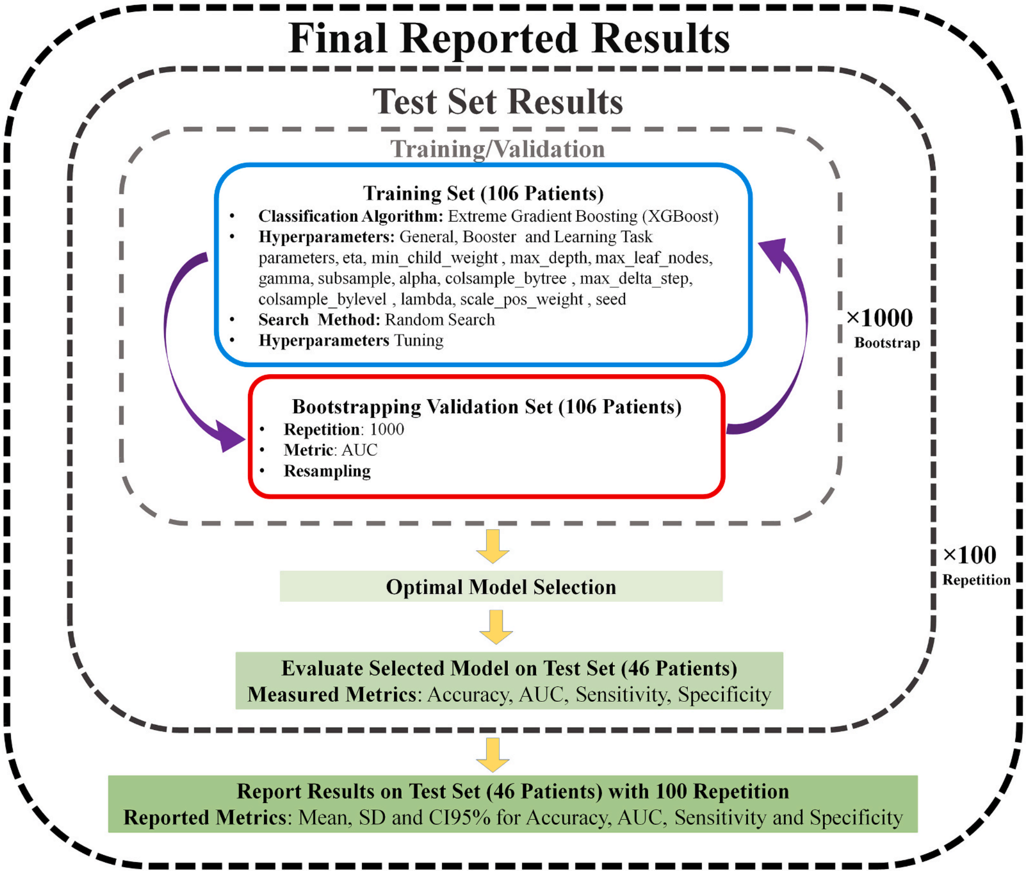

Fig. 3. Flowchart of the training and test steps implemented in the current study.

2.2. *Clinical data*

2.2.1. *Demographics, history and clinical data*

Gender, age, weight, height, BMI, past medical history of comorbidities (i.e. diabetes, hypertension, ischemic heart disease, and cancer), history of smoking, initial vital signs, including respiratory rate (RR), O_2 saturation (O2Sat), pulse rate (PR), systolic blood pressure (SBP), diastolic blood pressure (DBP), temperature in degrees Celsius (T) and the level of consciousness were obtained and recorded [6,41–43].

2.2.2. *Laboratory data*

Upon admission, the results of laboratory tests were extracted from patient medical records. These included aspartate aminotransferase in U/L (AST), alanine aminotransferase (ALT) in U/L, alkaline phosphatase (ALP) in U/L, total and direct bilirubin (T.Bill and D.Bill, respectively) in mg/dL, hemoglobin (HB) in g/dL, white blood cells (WBC) in/mm^3, venous blood gas analysis of acidity (PH), carbon dioxide concentration (PCO2), and bicarbonate concentration (HCO3), C-reactive protein in mg/L (CRP), platelet count in/mm^3 (Plt), blood creatinine level in mg/dL (Cr), blood urea nitrogen (BUN) in mg/dL, prothrombin time (PT) in seconds, partial thromboplastin time (PTT) in seconds, prothrombin time normalized with the international normalized ratio (INR), procalcitonin levels (PCT) in ng/dL, and sodium and potassium (Na and K, respectively) in mEq/L. We also used the differential counts of neutrophils, lymphocytes, monocytes, and eosinophils in percentages (Neutr. Diff, Lymph.Diff, Mono.Diff, and Eosin.Diff, respectively) [6,41–43].

2.2.3. *Radiological scores*

To obtain radiological data, we designed a questionnaire layout (presented in Supplemental material) based on which the following information was gathered: (a) type of parenchymal abnormality, such as (i) ground-glass opacities (GGO) (ii) consolidation, (iii) reticular pattern, and (iv) mixed pattern; (b) axial and craniocaudal distribution; (c) pleural effusion; (d) pericardial effusion; and (e) emphysema [6,41–43]. In addition, we adapted the 6-zone segmentation, which includes upper, middle and lower zone of each lung [6,41–43]. Both left and right lung were divided into three zones including carina upper level, between the carina and inferior pulmonary vein, and below the inferior pulmonary vein level [6,41–43]. Then, we separately evaluated each zone involvement and scored between 0 and 4 (0: no involvement, 1: 1%–25% involved, 2: 26%–50% involved, 3: 51%–75% involved, and 4: 76%–100% involved) [6,41–46]. The total involvement score (Inv. Score) was calculated by summing up different zones scores. All radiological scores were assigned by consensus of two experienced radiologists to report CT scan findings and a third senior radiologist settled any discordance/dispute between the two [6,41–43].

2.3. *CT imaging*

CT scanning with breath holding was performed on a 16 detector-row Brilliance 16CT scanner (Philips Medical Systems, Best, the Netherlands) using the following scanning parameters: A tube voltage of 100 KVp was used for patients with BMI $\leq$ 30 (111 patients) whereas 120 KVp was used for patients with BMI $>$ 30 (41 patients); 45 mA tube current; 16 $\times$ 1.5 mm collimation; 0.5 s rotation time; pitch of 1.0; and 35 cm field-of-view [6,41–43]. Low quality CT images owing to patient bulk motion, severe respiratory motion, or when the axial coverage was less than the total lungs were excluded.

2.4. *Image segmentation*

Two anatomical segmentations were performed, namely 1) whole

Table 2
Descriptive statistics (mean ± STD) of continues clinical features collected for the training/validation and test sets.

Continues Features	Training/ Validation	Test Set	p-value
Lesion Volume	280 ± 260	260 ± 230	0.51
Lung Volume	1300 ± 300	1300 ± 300	0.92
Lesion Lung Ratio	0.22 ± 0.22	0.21 ± 0.18	0.70
Age	62 ± 17	60 ± 15	0.53
Weight	77 ± 15	78 ± 16	0.18
Height	170 ± 9.7	170 ± 9.5	0.54
BMI	28 ± 4.7	28 ± 5.8	0.32
O2 Saturation (O2Sat)	90 ± 7.8	87 ± 10	0.66
Systolic Blood Pressure (SBP)	130 ± 23	120 ± 24	0.76
Diastolic Blood Pressure (DBP)	78 ± 14	76 ± 12	0.60
Respiratory Rate (RR)	20 ± 4.7	22 ± 7.3	0.39
Pulse Rate (PR)	94 ± 20	93 ± 13	0.08
Temperature in Celsius Degree (T)	37 ± 1	37 ± 0.93	0.61
HB	13 ± 2.9	12 ± 2.8	0.90
White Blood Cells (WBCs)	9000 ± 17000	9900 ± 8000	0.18
Platelet Count in/mm3 (Plt)	180000 ± 96000	210000 ± 110000	0.65
Lymphocyte Diff	19 ± 13	20 ± 13	0.62
Neutrophile Diff	73 ± 16	71 ± 16	0.67
Monocyte Diff	5.9 ± 3.4	6.7 ± 2.9	0.82
Eosinophile Diff	1.7 ± 2.6	1.6 ± 1.1	0.19
C-reactive Protein in mg/L (CRP)	64 ± 46	66 ± 40	0.45
Blood Creatinine Level in mg/dL (Cr)	1.3 ± 1	1.7 ± 1.7	0.18
BUN	24 ± 23	28 ± 26	0.84
AST	82 ± 220	54 ± 43	0.45
ALT	53 ± 160	38 ± 47	0.75
ALP	250 ± 250	180 ± 110	0.52
Sodium in mEq/L (Na)	140 ± 18	140 ± 3.6	0.39
Potassium in mEq/L (K)	4.6 ± 0.75	4.7 ± 0.72	0.96
PT	18 ± 10	16 ± 4.9	0.87
PTT	28 ± 11	27 ± 7.6	0.27
INR	1.6 ± 1	1.3 ± 0.43	0.58
T.Bill	2.1 ± 5	1.6 ± 2.6	0.50
D.Bill	0.91 ± 2.7	0.42 ± 0.26	0.75
PH	7.4 ± 0.08	7.4 ± 0.1	0.89
PCO2	40 ± 8.8	41 ± 13	0.07
HCO3	24 ± 5.7	24 ± 5.7	0.16
Total Invasive Score (Total. Inv.Score)	6.4 ± 4	7.2 ± 4.9	0.88

lung (Lung) and 2) COVID-19 lesions (Lesion). All segmentations were performed by a radiologist (12 years experience) using the 3D slicer software v4.8.1 [47].

2.5. Image preprocessing and feature extraction

All CT images were interpolated to isotropic voxel and re-sampled to 1 × 1 × 1 mm^3 [48]. Subsequently, bin discretization to 64gray levels were performed for radiomics analysis [48]. For feature extraction, first-order statistics (19 FOS features), shape-based (16 shape features), gray-level co-occurrence matrix (GLCM 23 features), gray-level run length matrix (16 GLRLM features), gray-level size zone matrix (16 GLSZM features), neighboring gray tone difference matrix (5 NGTDM features), and gray level dependence matrix (14 GLDM features) features were extracted [48,49]. Feature extraction was performed using PyRadiomics [49] v2.1.2 python-based software package, which was standardized through the Image Biomarker Standardization Initiative (IBSI) [48]. Full details about the feature categories are provided in Table 1. We also constructed 15 new shape features through division of lesion shape features by whole lung shape features to extract *relative* shape features.

Table 3
Descriptive statistics (frequency and percent) of discrete (categorical) clinical features in the training/validation and test sets.

Categorical Features		Training/ Validation (frequency in %)	Test (frequency in %)	p-value
Gender	F	37 (34.6%)	28 (62.2%)	0.15
	M	70 (65.4%)	17 (37.8%)	
ground-glass opacities (GGO)	0	4 (3.74%)	0	1.00
	1	49 (45.8%)	21 (46.7%)	
	2	54 (50.5%)	24 (53.3%)	
Consolidation	0	7 (6.54%)	7 (15.6%)	1.00
	1	53 (49.5%)	13 (28.9%)	
	2	47 (43.9%)	25 (55.6%)	
Reticular	0	36 (33.6%)	12 (26.7%)	0.58
	1	51 (47.7%)	25 (55.6%)	
	2	20 (18.7%)	8 (17.8%)	
Axial Distribution)Ax. Dist(	1	61 (57%)	23 (51.1%)	0.74
	2	2 (1.87%)	1 (2.22%)	
	3	44 (41.1%)	21 (46.7%)	
Coronal Distribution (CC. Dist)	1	4 (3.74%)	2 (4.44%)	0.37
	2	36 (33.6%)	16 (35.6%)	
	3	67 (62.6%)	27 (60%)	
Number of Involved Zones (Num.Zones. Involved)	1	3 (2.8%)	1 (2.22%)	0.79
	2	9 (8.41%)	3 (6.67%)	
	3	6 (5.61%)	4 (8.89%)	
	4	9 (8.41%)	5 (11.1%)	
	5	20 (18.7%)	5 (11.1%)	
	6	60 (56.1%)	27 (60%)	
Pleural Effusion (Pleural. Eff)	0	78 (72.9%)	36 (80%)	0.46
	1	29 (27.1%)	9 (20%)	
Pericardial Effusion (Pericardial.Eff)	0	88 (82.2%)	37 (82.2%)	1.00
	1	19 (17.8%)	8 (17.8%)	
Emphysema	0	79 (73.8%)	34 (75.6%)	0.61
	1	28 (26.2%)	11 (24.4%)	
Cardiomegaly	0	49 (45.8%)	22 (48.9%)	1.00
	1	58 (54.2%)	23 (51.1%)	
Diabetes	0	76 (71%)	35 (77.8%)	0.50
	1	31 (29%)	10 (22.2%)	
Hypertension) HTN (	0	71 (66.4%)	28 (62.2%)	1.00
	1	36 (33.6%)	17 (37.8%)	
Ischemic Heart Disease) IHD (	0	82 (76.6%)	37 (82.2%)	1.00
	1	25 (23.4%)	8 (17.8%)	
Cancerous	0	95 (88.8%)	42 (93.3%)	0.75
	1	12 (11.2%)	3 (6.67%)	
Smoking	1	94 (87.85%)	39 (86.67%)	0.55
	2	9 (8.41%)	4 (8.89%)	
	3	4 (3.74%)	2 (4.44%)	
Consciousness	0	2 (1.87%)	0	0.46
	1	1 (0.935%)	1 (2.22%)	
	2	9 (8.41%)	4 (8.89%)	
	3	95 (88.8%)	40 (88.89%)	
Mixed	0	50 (46.7%)	30 (66.7%)	0.57
	1	57 (53.3%)	15 (33.3%)	

2.6. Univariate analysis

We performed univariate analysis after normalization of each feature to Z-scores to determine the prognostic importance of each feature (clinical, radiological and radiomics). For continuous features, we performed Student's t-test and area under the ROC curve (AUC) analysis. The performance of categorical features was evaluated using the Chi-square test. We also applied false discovery rate (FDR) correction to the q-value (FDR adjusted p-value) to assess the significance of the features.

2.7. Multivariate machine learning analysis

The maximum relevance minimum redundancy (MRMR) algorithm [50] was used for feature selection. To this end, the maximum-relevance selection approach was employed to select features with maximal correlation to patients' outcome (alive or deceased status) and minimum-redundancy selection, thus ensuring minimal redundancy

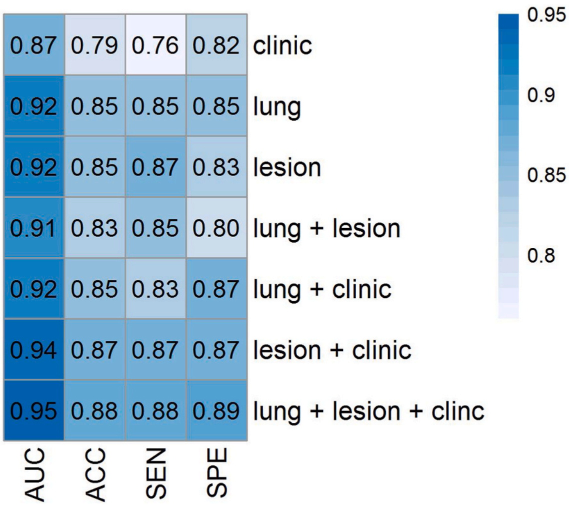

Fig. 4. Heat map of area under the curve (AUC), accuracy (ACC), sensitivity (SEN) and specificity (SPE) for different combinations of models.

Table 4
Mean and STD of area under the curve (AUC), accuracy (ACC), sensitivity (SNE) and specificity (SPE) in the test set for the different models studied.

Mean ± Sd	AUC	ACC	SEN	SPE
Clinical	0.87 ± 0.04	0.79 ± 0.05	0.76 ± 0.07	0.82 ± 0.08
Lung	0.92 ± 0.03	0.85 ± 0.04	0.85 ± 0.07	0.85 ± 0.06
Lesion	0.92 ± 0.03	0.85 ± 0.05	0.87 ± 0.06	0.83 ± 0.08
Lung + Lesion	0.91 ± 0.04	0.83 ± 0.05	0.85 ± 0.08	0.80 ± 0.09
Lung + Clinical	0.92 ± 0.03	0.85 ± 0.04	0.83 ± 0.06	0.87 ± 0.05
Lesion + Clinical	0.94 ± 0.03	0.87 ± 0.04	0.87 ± 0.07	0.87 ± 0.06
Lung + Lesion + Clinical	0.95 ± 0.03	0.88 ± 0.04	0.88 ± 0.06	0.89 ± 0.07

Table 5
Confidence interval (CI) of area under the curve (AUC), accuracy (ACC), sensitivity (SNE) and specificity (SPE) in the test set for the different models.

CI (lower-upper)	AUC	ACC	SEN	SPE
Clinical	0.86–0.87	0.78–0.80	0.74–0.77	0.81–0.84
Lung	0.91–0.92	0.84–0.86	0.84–0.86	0.84–0.87
Lesion	0.91–0.93	0.84–0.86	0.85–0.88	0.81–0.84
Lung + Lesion	0.90–0.91	0.82–0.84	0.84–0.87	0.79–0.82
Lung + Clinical	0.92–0.93	0.84–0.86	0.82–0.84	0.86–0.88
Lesion + Clinical	0.93–0.95	0.86–0.88	0.86–0.89	0.85–0.88
Lung + Lesion + Clinical	0.95–0.96	0.88–0.89	0.87–0.90	0.87–0.90

among features [50]. The eXtreme Gradient Boosting (XGBoost) machine learning algorithm [51] which is an ensemble learning algorithms based on different decision trees was adopted for classification. Feature selection and classification were performed using praznik and caret R packages,[2] respectively.

2.8. Data modeling and univariate analysis

We developed various prognostic models using the collected data and the adopted classification method. Our models were: 1) Clinical (pre-clinical, lab and radiological data), 2) Lung radiomics (radiomic features extracted from the whole lung), 3) Lesion radiomics (radiomic features extracted from lesions), 4) Lung + Lesion (combined radiomic features extracted from whole lung and lesions), 5) Lung + Clinical (combined radiomic features extracted from whole lung, clinical and radiological data), 6) Lesion + Clinical (combined radiomic features extracted from lesions, clinical and radiological data) and 7) Lung + Lesion + Clinical (combined radiomic features extracted from whole lung, lesions, clinical and radiological data). For model validation, 106 patients were used as the training/validation dataset whereas the remaining 46 patients were used as the test (unseen and untouched during training) dataset. The ROC, AUC, accuracy (ACC), sensitivity (SEN) and specificity (SPE) were used to assess the prognostic performance of the models. The different steps followed are summarized in Fig. 3:

1. The model was trained using 106 patients' data. Yet, to find the optimal hyperparameters of models, we used bootstrap resampling with 1000 repetitions. Bootstrap techniques were used for XGBoost hyperparameters tunning (using the random search method) implemented with 1000 repetitions.
2. After tuning and optimizing the models based on AUC, we selected the optimal model.
3. The optimal model was tested on the test set (test datasets untouched/unseen during bootstrapping). We calculated Accuracy, AUC, Sensitivity, and Specificity for the optimal model on the test datasets.
4. Steps 1–3 were repeated 100 times to ensure the repeatability of the results.
5. The Mean, SD and CI95% were calculated from step 4 for Accuracy, AUC, Sensitivity, Specificity metrics.
6. Clinical, radiomics and combined models were statistically evaluated using the results of step 5.

We repeatedly trained a bootstrapped model with 1000 repetition (on 106 patients dataset) and tested on an independent dataset for 100 times to make sure that the results are repeatable for different models. All results were reported on 46 test sets (unseen during model training by bootstrap) by 100 times repetitions. The mean, standard deviation and 95% confidence interval (CI) were reported for each model for 100 times repetitions of the whole process. After data normality test using Kolmogorov-Smirnov normality test, we used Wilcoxon signed-rank test to determine significant differences between the models. A p-value < 0.05 was used as a criterion for statistically significant differences. All statistical analysis was performed using R 3.6.3 software.

3. Results

3.1. Patient population

Following application of inclusion and exclusion criteria, 152 patients including 87 males and 65 females were retained from an initial triage of 545 patients. Forty patients with a mean age of 65.7 years had critical conditions and eventually died, whereas 112 cases with a mean age of 59.5 years fully recovered from COVID-19. The flowchart in Fig. 2 shows the number of excluded, included, recovered and deceased patients. The details of the descriptive statistics of continuous and categorical features of patients are presented in Tables 2 and 3 for the training/validation and test sets (unseen and untouched during training).

3.2. Univariate analysis

Our univariate analysis of clinical features is shown in Supplemental Figures 1 and 2 as categorical and continuous features in terms of AUC,

---

[2] https://www.r-project.org.

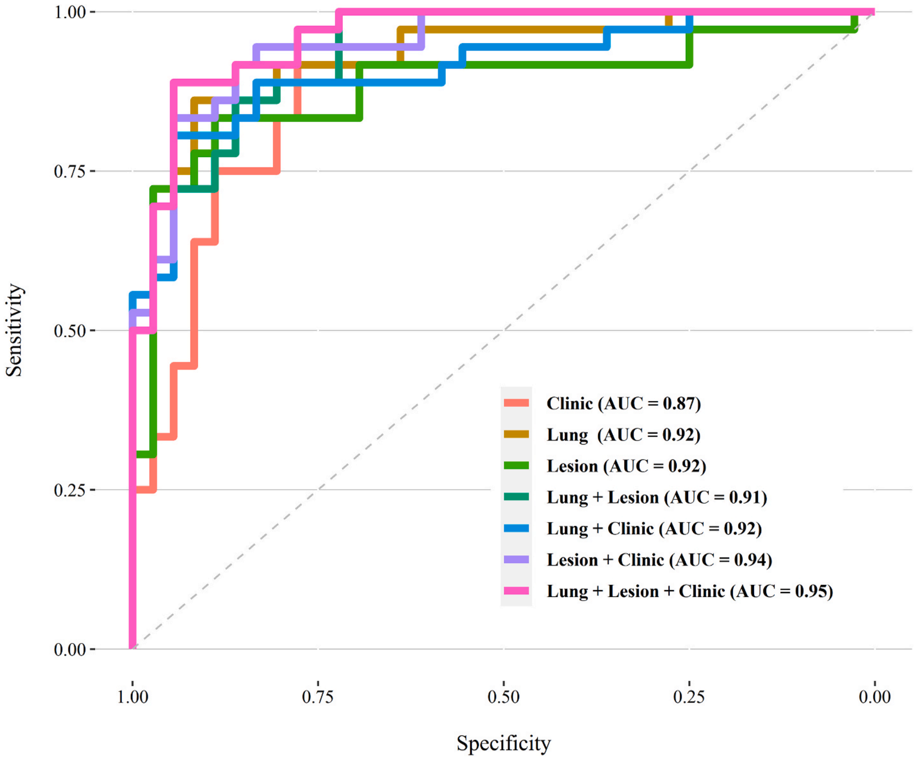

Fig. 5. ROC curve of the different models in the test sets.

p- and q-values. In this regard, clinical features, including BUN (AUC = 0.73) and oxygen saturation (AUC = 0 0.71), monocyte (AUC = 0.70) and a number of involved zones (AUC = 0.70) were identified as most prognostic features. Amongst continuous clinical features, systolic blood pressure, diastolic blood pressure, hemoglobin, platelet, lymphocyte, neutrophil, monocyte, had a q-value < 0.05. Amongst discrete (categorical) clinical features, smoking, cancerous, consciousness and total involvement score proved to be statistically significant features (p-value < 0.05) between two alive and deceased group.

For univariate radiomics analysis, the results are displayed in Supplemental Figures 3 and 4. Amongst lung radiomic features, SAHGLE (AUC = 0.70) and HGLZE (AUC = 0.67) from GLSZM, JA and SA from GLCM, Busyness from NGTDM and Median from FO (AUC = 0.67) were found as most prognostic features. Amongst lesion radiomic features, RLNU from GLRLM, HGLZE from GLSZM, DNU from GLDM, Range from FO and Volume from Shape (AUC = 0.73) had the highest performance with significant q-value after FDR correction.

3.3. Models

Importance features selected by the MRMR algorithm were reported for each model in Supplemental Table 2. Fig. 4 depicts the heat map of AUC, ACC, SEN and SPE for different combinations of models. The mean (STD) and confidence interval (CI) for AUC, ACC, SEN and SPE for the developed models (test set) are summarized in Tables 4 and 5, respectively. Our results indicated that the combined model (Lung + Lesion + Clinical) had the highest prognostic capability with AUC = 0.95 ± 0.02, ACC = 0.88 ± 0.04, SEN = 0.88 ± 0.06 and SPE = 0.89 ± 0.07. The 95% CI for these parameters were 0.95–0.96, 0.88–0.89, 0.87–0.90 and 0.87–0.90, respectively.

The ROC curve and boxplot of these models for the test set are shown in Figs. 5 and 6, respectively. In the boxplots, significant differences among the models can be observed. To compare the models in terms of significant changes in AUC, ACC, SEN and SPE, p-value plots are shown in Fig. 7. It can be seen that the combined Lung + Lesion + Clinical model has significant AUC differences ($p < 0.05$) relative to other models. The model was also significantly different in terms of ACC with respect to all models. With respect to SPE, all models had significant differences, except Lung + Clinical model, whereas for SEN, all models were significantly different, except the Lesion + Clinical model. In terms of AUC, except Lung and Lesion, Lung + Clinical and Lung, Lung + Lesion and Lung models as well as Lung + Clinical and Lesion models were significantly different ($p < 0.05$).

4. Discussion

A novel approach for prognostication of COVID-19 patients using different image-derived features, including semantic, radiomics and clinical data (demographics and history, laboratory tests and visual scoring of CT by radiologists) was presented in this work. We demonstrated that clinical and quantitative radiomic features, alone or in combination, can be used as potential biomarkers for the prediction of survival in COVID-19 patients. Although some radiomic studies have been conducted in the framework of COVID-19, this is to the best of our knowledge, the first study reporting on the use of advanced combined models for prognosis survival analysis.

We extracted two categories of radiomic features from whole lung and lung lesions. The aim was to assess how the extracted radiomic features might be used as different prognostic parameters. Decoding heterogeneity is among the aims of radiomics analysis. Hence, since the delineated lesions and whole lungs have different characteristics, they could serve as different markers. Conversely, combining these features along with other clinical parameters provides more variables for developing more predictive models. In previous lung radiomic studies, adding clinical data to radiomic signatures improved model performance. A study by Chen et al. [52] demonstrated that adding clinical data, such as smoking history, enabled to slightly improve performance for differentiating peripherally-located small cell lung cancer from non-small cell lung cancer using CT radiomic features.

Univariate analysis showed that some clinical parameters might be predictive. Although for single clinical parameters, the highest AUCs were achieved for BUN, oxygen saturation, monocyte count and a

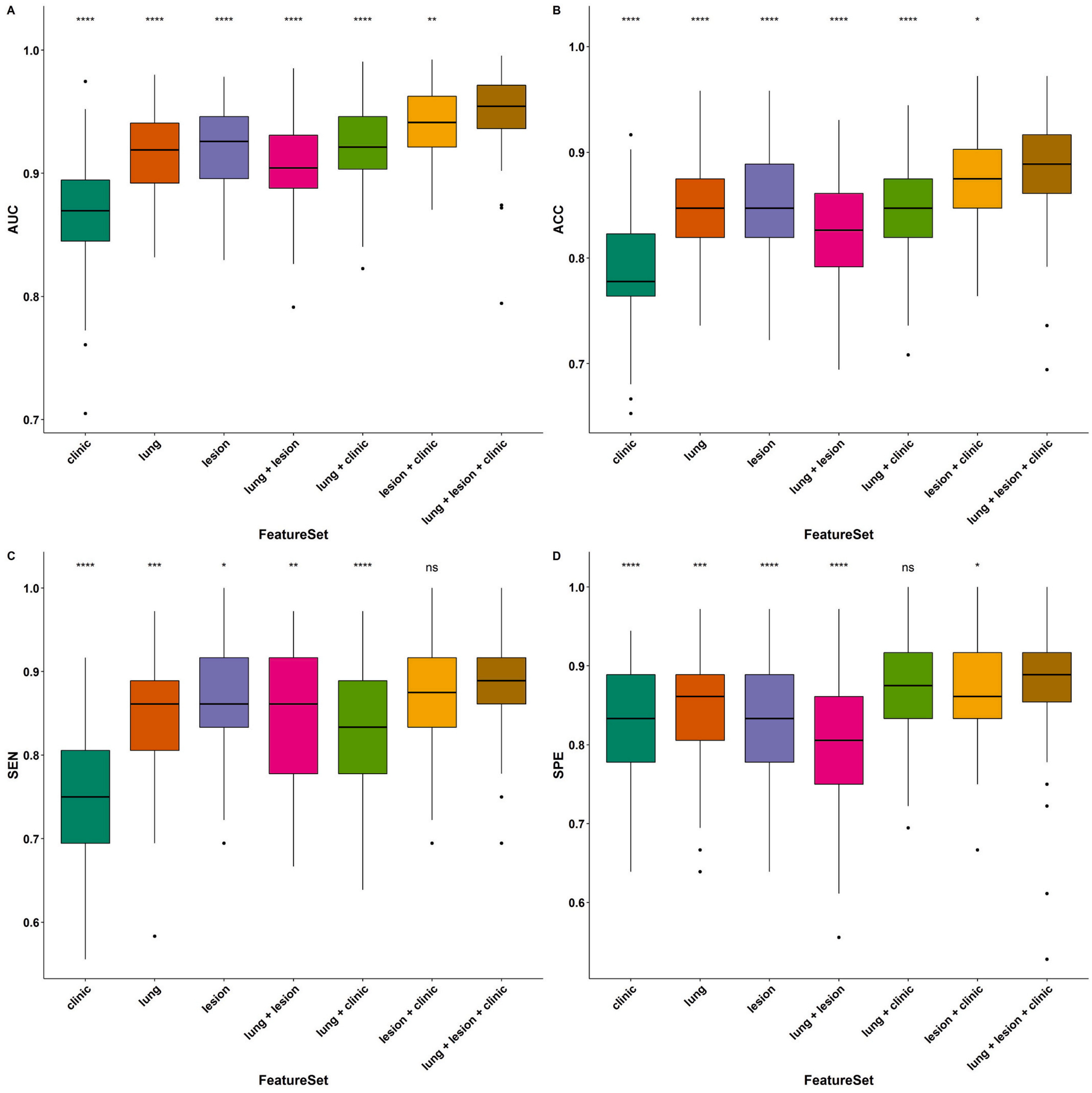

Fig. 6. Box plot of the area under the curve (AUC), accuracy (ACC), sensitivity (SEN) and specificity (SPE) for different combinations of models. P-values comparing differences in values with respect to the Lung + Lesion + Clinical model are shown. Not significant (ns): $p > 0.05$, *: $p \leq 0.05$, **: $p \leq 0.01$, ***: $p \leq 0.001$ and ****: $p \leq 0.0001$.

number of involved zones. These findings were congruent with previous studies. Several studies have suggested that increased BUN can be attributed to acute kidney injury during the course of the disease, which can be a cause of adverse effects [53–55]. Colombi et al. [56] reported lung involvement area and hypoxia as reliable predictors of ICU admission and mortality among COVID-19 patients. Conversely, we believe that the fact that the results on monocyte count can be an outcome predictor is the consequence of our sample size as Zeng et al. [57] did not report significant differences between severe and non-severe patients in a population of 3090 patients from 15 different studies. With respect to single imaging measures, we observed that several radiomic features were predictive in both lesion and whole lung delineations. When comparing these two feature categories, it appeared that whole lung features have higher AUCs. A recent study by Tan et al. [58] demonstrated the predictive value of non-focus area of CT images to distinguish different clinical types of COVID-19 pneumonia. In our study, whole lung features provided more relevant characteristics of the disease in COVID-19 patients. Extracting radiomic features from infected and non-infected regions provided a more accurate prognostic model.

On the modeling of prognosis prediction, we observed that the combined model including all measures had the highest performance and had significant differences with other models. In addition, we showed that other models have similar behavior, although there were

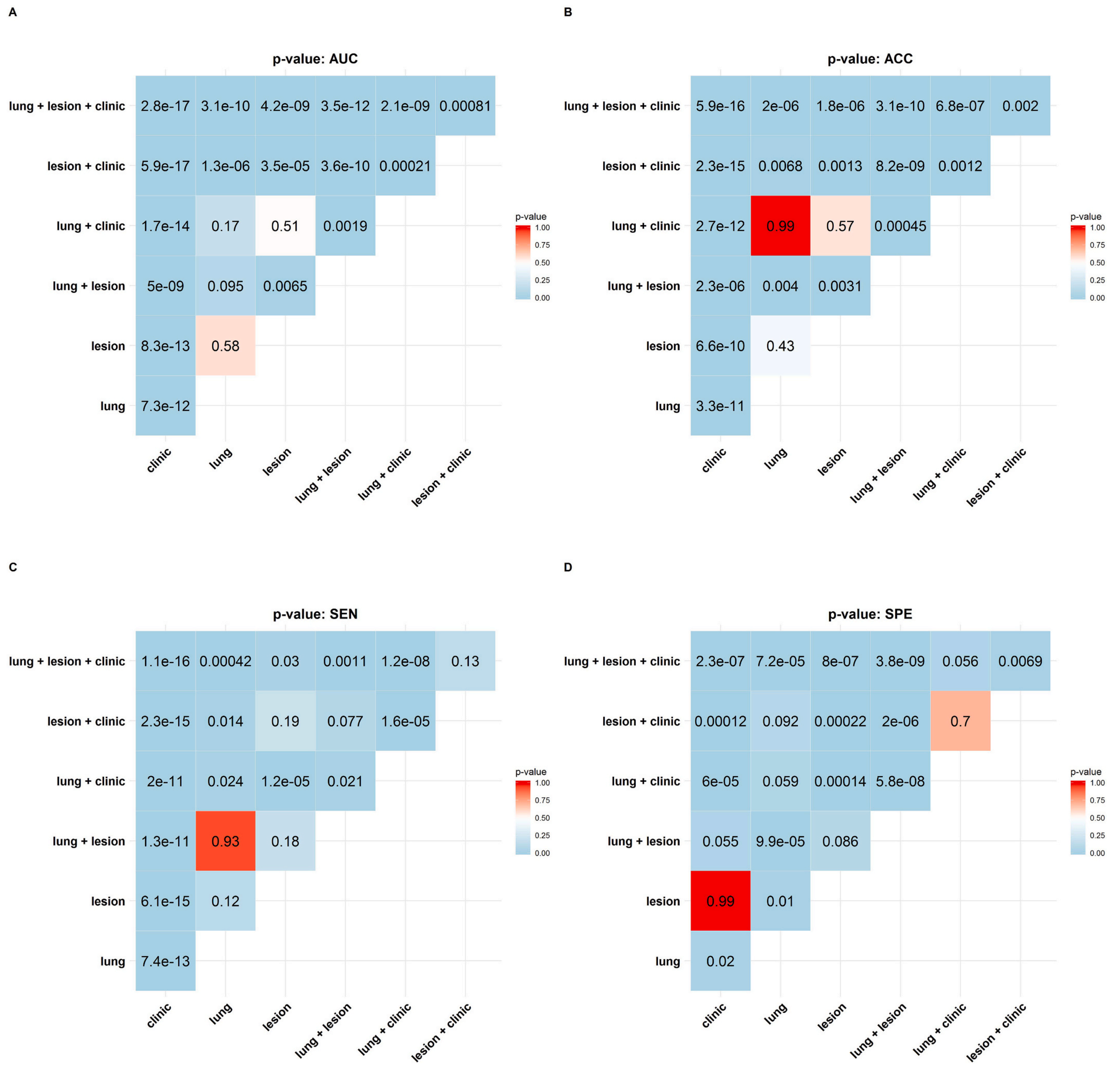

Fig. 7. P-values for the comparison between the different models with respect to the area under the curve (AUC), accuracy (ACC), sensitivity (SEN) and specificity (SPE).

significant differences among them. For both radiomic models, the AUC had a range varying from 0.91 to 0.93. However, when they were combined with clinical features, the AUC improved from 0.91 to 0.93 to 0.95–0.96. These results indicated that the combined models provided more accurate information. In addition, compared to univariate radiomics analysis, multivariate modeling results in more reliable results. It should be emphasized that in predictive modeling, the variables are the heart of the model, although the classifiers have a critical role [59,60]. In this work, we used a classifier with a wide range of features.

A wide range of image analysis algorithms combined with machine learning techniques were recently designed for COVID-19 detection, diagnosis and prognosis. Li et al. [61] applied artificial intelligence algorithms to distinguish COVID-19 from community acquired pneumonia on chest CT. They developed a deep learning model, COVID-19 detection neural network (COVNet), to extract visual features from volumetric chest CT examinations for the detection of COVID-19 and compared them to community acquired pneumonia and other non-pneumonia images. Their model achieved a sensitivity and specificity of 90% and 96%, respectively, with an AUC of 0.96. Although deep learning models have achieved a high predictive/prognostic performance, their mechanisms of action are not fully understood [62]. Yet, radiomic features may provide more reliable results because they capture tissue characteristics. Hence, studies have indicated that these markers could decode the biological properties of the tissues [63,64]. In this regard, we believe that our results could be exploited reliably in clinical practice.

Although the presented results are important, this study inherently bears a number of limitations. First, the sample size is low and there is a lack of external validation set from different centers. Further clinical studies are needed to verify our results with larger clinical databases. Second, therapeutic strategies for patients were not considered in this study. Including treatment parameters in the models will provide more reliable results. Third, although our imaging and radiomics settings were similar for all patients, we suggest to assess radiomic features reproducibility before clinical adoption. Image segmentation was performed by an experienced radiologist only once, and as such, it was not possible to estimate the intra-observer variability and repeatability of the segmentations. Forth, we only tested one feature selection and classifier algorithms. As there is no one-fits-all machine learning algorithm, different combinations of feature selectors and classifiers result in different performance. Future studies should focus on evaluating different algorithms and comparing their performance [65,66]. Various inclusion and exclusion criteria were applied retrospectively to the datasets, which decreased the number of cases. Patients with severe motion artifacts, which is inevitable in some non-cooperative or unstable patients, were excluded. This might impact the generalizability of the obtained results. Future studies should use a more heterogeneous dataset in terms of CT image quality to ensure the generalizability of the model.

5. Conclusion

We demonstrated that the combination of radiomic features, clinical and radiological data could be used to effectively predict survival in COVID-19 patients. To the best of our knowledge, this is the first study applying such methodology for COVID-19 prognosis survival modeling. We also demonstrated that there are a number of individual predictive clinical or imaging features having the potential to be used in routine clinical practice for more accurate management of COVID-19 patients.

Declaration of competing interest

The authors declare that they have no conflict of interest.

Acknowledgments

This work was supported by the Swiss National Science Foundation under grant SNRF 320030_176052 and International affairs of Tehran University of Medical Sciences under grant number 99-2-163-49381.

Appendix A. Supplementary data

Supplementary data to this article can be found online at https://doi.org/10.1016/j.compbiomed.2021.104304.

References

[1] N. Zhu, D. Zhang, W. Wang, X. Li, B. Yang, J. Song, X. Zhao, B. Huang, W. Shi, R. Lu, P. Niu, F. Zhan, X. Ma, D. Wang, W. Xu, G. Wu, G.F. Gao, W. Tan, I. China Novel Coronavirus, T. Research, A novel coronavirus from patients with pneumonia in China, 2019, N. Engl. J. Med. 382 (2020) 727–733.

[2] Z. Wu, J.M. McGoogan, Characteristics of and important lessons from the coronavirus disease 2019 (COVID-19) outbreak in China: summary of a report of 72314 cases from the Chinese Center for Disease Control and Prevention, J. Am. Med. Assoc. 323 (13) (2020) 1239–1242.

[3] Y. Fang, H. Zhang, J. Xie, M. Lin, L. Ying, P. Pang, W. Ji, Sensitivity of chest CT for COVID-19: comparison to RT-PCR, Radiology (2020) 200432.

[4] T. Ai, Z. Yang, H. Hou, C. Zhan, C. Chen, W. Lv, Q. Tao, Z. Sun, L. Xia, Correlation of chest CT and RT-PCR testing in coronavirus disease 2019 (COVID-19) in China: a report of 1014 cases, Radiology (2020) 200642.

[5] H.X. Bai, B. Hsieh, Z. Xiong, K. Halsey, J.W. Choi, T.M.L. Tran, I. Pan, L.-B. Shi, D.-C. Wang, J. Mei, Performance of radiologists in differentiating COVID-19 from viral pneumonia on chest CT, Radiology (2020) 200823.

[6] B. Khosravi, L. Aghaghazvini, M. Sorouri, S. Naybandi Atashi, M. Abdollahi, H. Mojtabavi, M. Khodabakhshi, F. Motamedi, F. Azizi, Z. Rajabi, A. Kasaeian, A. R. Sima, A.H. Davarpanah, A.R. Radmard, Predictive value of initial CT scan for various adverse outcomes in patients with COVID-19 pneumonia, Heart Lung 50 (1) (2020) 13–20.

[7] L. Büttner, A. Aigner, F.N. Fleckenstein, C.M. Hamper, M. Jonczyk, B. Hamm, O. Scholz, G. Böning, Diagnostic value of initial chest CT findings for the need of ICU treatment/intubation in patients with COVID-19, Diagnostics 10 (2020).

[8] V. Kumar, Y. Gu, S. Basu, A. Berglund, S.A. Eschrich, M.B. Schabath, K. Forster, H. J. Aerts, A. Dekker, D. Fenstermacher, D.B. Goldgof, L.O. Hall, P. Lambin, Y. Balagurunathan, R.A. Gatenby, R.J. Gillies, Radiomics: the process and the challenges, Magn. Reson. Imaging 30 (2012) 1234–1248.

[9] S.S. Yip, H.J. Aerts, Applications and limitations of radiomics, Phys. Med. Biol. 61 (2016) R150–R166.

[10] S. Mostafaei, H. Abdollahi, S.K. Dehkordi, I. Shiri, A. Razzaghdoust, S.H. Z. Moghaddam, A. Saadipoor, F. Koosha, S. Cheraghi, S.R. Mahdavi, CT imaging markers to improve radiation toxicity prediction in prostate cancer radiotherapy by stacking regression algorithm, La radiologia medica 125 (2020) 87–97.

[11] M. Nazari, I. Shiri, G. Hajianfar, N. Oveisi, H. Abdollahi, M.R. Deevband, M. Oveisi, H. Zaidi, Noninvasive Fuhrman grading of clear cell renal cell carcinoma using computed tomography radiomic features and machine learning, Radiol. Med. (2020) 1–9.

[12] K.K. Yan, X. Wang, W.W.T. Lam, V. Vardhanabhuti, A.W.M. Lee, H.H. Pang, Radiomics analysis using stability selection supervised component analysis for right-censored survival data, Comput. Biol. Med. 124 (2020) 103959.

[13] G.S. Tandel, A. Balestrieri, T. Jujaray, N.N. Khanna, L. Saba, J.S. Suri, Multiclass magnetic resonance imaging brain tumor classification using artificial intelligence paradigm, Comput. Biol. Med. 122 (2020) 103804.

[14] D. Molina, J. Pérez-Beteta, A. Martínez-González, J. Martino, C. Velásquez, E. Arana, V.M. Pérez-García, Influence of gray level and space discretization on brain tumor heterogeneity measures obtained from magnetic resonance images, Comput. Biol. Med. 78 (2016) 49–57.

[15] L.F. Machado, P.C. Elias, A.C. Moreira, A.C. Dos Santos, L.O.M. Junior, MRI radiomics for the prediction of recurrence in patients with clinically non-functioning pituitary macroadenomas, Comput. Biol. Med. 124 (2020) 103966.

[16] S. Rastegar, M. Vaziri, Y. Qasempour, M. Akhash, N. Abdalvand, I. Shiri, H. Abdollahi, H. Zaidi, Radiomics for classification of bone mineral loss: a machine learning study, Diagnostic and Interventional Imaging 101 (9) (2020) 599–610.

[17] R. Paul, M. Schabath, R. Gillies, L. Hall, D. Goldgof, Convolutional Neural Network ensembles for accurate lung nodule malignancy prediction 2 years in the future, Comput. Biol. Med. 122 (2020) 103882.

[18] W. Sun, B. Zheng, W. Qian, Automatic feature learning using multichannel ROI based on deep structured algorithms for computerized lung cancer diagnosis, Comput. Biol. Med. 89 (2017) 530–539.

[19] Y. Kurata, M. Nishio, A. Kido, K. Fujimoto, M. Yakami, H. Isoda, K. Togashi, Automatic segmentation of the uterus on MRI using a convolutional neural network, Comput. Biol. Med. 114 (2019) 103438.

[20] J. Somasekar, P. Pavan Kumar Visulaization, A. Sharma, G. Ramesh, Machine learning and image analysis applications in the fight against COVID-19 pandemic: datasets, research directions, challenges and opportunities,, Mater. Today Proc. (2020), https://doi.org/10.1016/j.matpr.2020.09.352. In press.

[21] P. Meyer, V. Noblet, C. Mazzara, A. Lallement, Survey on deep learning for radiotherapy, Comput. Biol. Med. 98 (2018) 126–146.

[22] S. Bonte, I. Goethals, R. Van Holen, Machine learning based brain tumour segmentation on limited data using local texture and abnormality, Comput. Biol. Med. 98 (2018) 39–47.

[23] L. Li, K. Wang, X. Ma, Z. Liu, S. Wang, J. Du, K. Tian, X. Zhou, K. Sun, Y. Lin, Radiomic analysis of multiparametric magnetic resonance imaging for differentiating skull base chordoma and chondrosarcoma, Eur. J. Radiol. 118 (2019) 81–87.

[24] W. Yanling, G. Duo, G. Zuojun, S. Zhongqiang, W. Yankai, L. Shan, C. Hongying, Radiomics nomogram analyses for differentiating pneumonia and acute paraquat lung injury, Sci. Rep. 9 (2019) 1–9.

[25] B. Wang, M. Li, H. Ma, F. Han, Y. Wang, S. Zhao, Z. Liu, T. Yu, J. Tian, D. Dong, Computed tomography-based predictive nomogram for differentiating primary progressive pulmonary tuberculosis from community-acquired pneumonia in children, BMC Med. Imag. 19 (2019) 63.

[26] Q. Cai, S.Y. Du, S. Gao, G.L. Huang, Z. Zhang, S. Li, X. Wang, P.L. Li, P. Lv, G. Hou, L.N. Zhang, A model based on CT radiomic features for predicting RT-PCR becoming negative in coronavirus disease 2019 (COVID-19) patients, BMC Med. Imag. 20 (2020) 118.

[27] S. Karakanis, G. Leontidis, Lightweight deep learning models for detecting COVID-19 from chest X-ray images, Comput. Biol. Med. 130 (2021) 104181.

[28] J.S. Suri, A. Puvvula, M. Biswas, M. Majhail, L. Saba, G. Faa, I.M. Singh, R. Oberleitner, M. Turk, P.S. Chadha, A.M. Johri, J.M. Sanches, N.N. Khanna, K. Viskovic, S. Mavrogeni, J.R. Laird, G. Pareek, M. Miner, D.W. Sobel, A. Balestrieri, P.P. Sfikakis, G. Tsoulfas, A. Protogerou, D.P. Misra, V. Agarwal, G. D. Kitas, P. Ahluwalia, R. Kolluri, J. Teji, M.A. Maini, A. Agbakoba, S.K. Dhanjil, M. Sockalingam, A. Saxena, A. Nicolaides, A. Sharma, V. Rathore, J.N. A. Ajuluchukwu, M. Fatemi, A. Alizad, V. Viswanathan, P.R. Krishnan, S. Naidu, COVID-19 pathways for brain and heart injury in comorbidity patients: a role of medical imaging and artificial intelligence-based COVID severity classification: a review, Comput. Biol. Med. 124 (2020) 103960.

[29] D. Barh, S. Tiwari, M.E. Weener, V. Azevedo, A. Góes-Neto, M.M. Gromiha, P. Ghosh, Multi-omics-based identification of SARS-CoV-2 infection biology and candidate drugs against COVID-19, Comput. Biol. Med. 126 (2020) 104051.

[30] T. Ozturk, M. Talo, E.A. Yildirim, U.B. Baloglu, O. Yildirim, U. Rajendra Acharya, Automated detection of COVID-19 cases using deep neural networks with X-ray images, Comput. Biol. Med. 121 (2020) 103792.

[31] A. Amyar, R. Modzelewski, H. Li, S. Ruan, Multi-task deep learning based CT imaging analysis for COVID-19 pneumonia: classification and segmentation, Comput. Biol. Med. 126 (2020) 104037.

[32] H. Burdick, C. Lam, S. Mataraso, A. Siefkas, G. Braden, R.P. Dellinger, A. McCoy, J.-L. Vincent, A. Green-Saxena, G. Barnes, J. Hoffman, J. Calvert, E. Pellegrini, R. Das, Prediction of respiratory decompensation in Covid-19 patients using machine learning: the READY trial, Comput. Biol. Med. 124 (2020) 103949.

[33] A.A. Ardakani, A.R. Kanafi, U.R. Acharya, N. Khadem, A. Mohammadi, Application of deep learning technique to manage COVID-19 in routine clinical practice using CT images: results of 10 convolutional neural networks, Comput. Biol. Med. 121 (2020) 103795.

[34] I. Shiri, A. Akhavanallaf, A. Sanaat, Y. Salimi, D. Askari, Z. Mansouri, S. P. Shayesteh, M. Hasanian, K. Rezaei-Kalantari, A. Salahshour, S. Sandoughdaran, H. Abdollahi, H. Arabi, H. Zaidi, Ultra-low-dose chest CT imaging of COVID-19 patients using a deep residual neural network, Eur. Radiol. (2020) 1–12.

[35] H. Chao, X. Fang, J. Zhang, F. Homayounieh, C.D. Arru, S.R. Digumarthy, R. Babaei, H.K. Mobin, I. Mohseni, L. Saba, A. Carriero, Z. Falaschi, A. Pasche, G. Wang, M.K. Kalra, P. Yan, Integrative analysis for COVID-19 patient outcome prediction, Med. Image Anal. 67 (2021) 101844.

[36] F. Shi, J. Wang, J. Shi, Z. Wu, Q. Wang, Z. Tang, K. He, Y. Shi, D. Shen, Review of artificial intelligence techniques in imaging data acquisition, segmentation and diagnosis for covid-19, IEEE Reviews in Biomedical Engineering 14 (2020) 4–15.

[37] X. Mei, H.C. Lee, K.Y. Diao, M. Huang, B. Lin, C. Liu, Z. Xie, Y. Ma, P.M. Robson, M. Chung, A. Bernheim, V. Mani, C. Calcagno, K. Li, S. Li, H. Shan, J. Lv, T. Zhao, J. Xia, Q. Long, S. Steinberger, A. Jacobi, T. Deyer, M. Luksza, F. Liu, B.P. Little, Z. A. Fayad, Y. Yang, Artificial intelligence-enabled rapid diagnosis of patients with COVID-19, Nat. Med. 26 (8) (2020) 1224–1228.

[38] J. Guiot, A. Vaidyanathan, L. Deprez, F. Zerka, D. Danthine, A.-N. Frix, M. Thys, M. Henket, G. Canivet, S. Mathieu, Development and Validation of an Automated Radiomic CT Signature for Detecting COVID-19, medRxiv, 2020.

[39] M. Fang, B. He, L. Li, D. Dong, X. Yang, C. Li, L. Meng, L. Zhong, H. Li, H. Li, CT radiomics can help screen the coronavirus disease 2019 (COVID-19): a preliminary study, Sci. China Inf. Sci. 63 (2020).

[40] G.S. Collins, J.B. Reitsma, D.G. Altman, K.G. Moons, Transparent reporting of a multivariable prediction model for individual prognosis or diagnosis (TRIPOD): the TRIPOD statement, BMJ 350 (2015) g7594.

[41] M. Sorouri, A. Kasaeian, H. Mojtabavi, A.R. Radmard, S. Kolahdoozan, A. Anushiravani, B. Khosravi, S.M. Pourabbas, M. Eslahi, A. Sirusbakht, M. Khodabakhshi, F. Motamedi, F. Azizi, R. Ghanbari, Z. Rajabi, A.R. Sima, S. Rad, M. Abdollahi, Clinical characteristics, outcomes, and risk factors for mortality in hospitalized patients with COVID-19 and cancer history: a propensity score-matched study, Infect. Agents Canc. 15 (2020) 74.

[42] A. Mansour, S.M. Sajjadi-Jazi, A. Kasaeian, B. Khosravi, M. Sorouri, F. Azizi, Z. Rajabi, F. Motamedi, A. Sirusbakht, M. Eslahi, H. Mojtabbavi, A.R. Sima, A. R. Radmard, M.R. Mohajeri-Tehrani, M. Abdollahi, Clinical characteristics and outcomes of diabetics hospitalized for COVID-19 infection: a single-centered, retrospective, observational study, Excli j 19 (2020) 1533–1543.

[43] A. Anoshiravani, H. Vahedi, S. Nasseri-Moghaddam, H. Fakheri, F. Mansour-Ghanaei, I. Maleki, H. Vosoghinia, M.R. Ghadir, A. Hormati, N. Aminisani, A supporting system for management of patients with inflammatory bowel disease during COVID-19 outbreak: Iranian experience-study protocol, Middle East Journal of Digestive Diseases (MEJDD) 12 (2020) 238–245.

[44] C. Li, D. Dong, L. Li, W. Gong, X. Li, Y. Bai, M. Wang, Z. Hu, Y. Zha, J. Tian, Classification of severe and critical COVID-19 using deep learning and radiomics, IEEE journal of biomedical and health informatics 24 (12) (2020) 3585–3594.

[45] B. Abbasi, R. Akhavan, A. Ghamari Khameneh, B. Zandi, D. Farrokh, M. Pezeshki Rad, A. Feyzi Laein, A. Darvish, B. Bijan, Evaluation of the relationship between inpatient COVID-19 mortality and chest CT severity score, Am. J. Emerg. Med. (2020). In press.

[46] G.C. Ooi, P.L. Khong, N.L. Müller, W.C. Yiu, L.J. Zhou, J.C. Ho, B. Lam, S. Nicolaou, K.W. Tsang, Severe acute respiratory syndrome: temporal lung changes at thin-section CT in 30 patients, Radiology 230 (2004) 836–844.

[47] A. Fedorov, R. Beichel, J. Kalpathy-Cramer, J. Finet, J.C. Fillion-Robin, S. Pujol, C. Bauer, D. Jennings, F. Fennessy, M. Sonka, J. Buatti, S. Aylward, J.V. Miller, S. Pieper, R. Kikinis, 3D slicer as an image computing platform for the quantitative imaging network, Magn. Reson. Imaging 30 (2012) 1323–1341.

[48] A. Zwanenburg, M. Vallières, M.A. Abdalah, H. Aerts, V. Andrearczyk, A. Apte, S. Ashrafinia, S. Bakas, R.J. Beukinga, R. Boellaard, M. Bogowicz, L. Boldrini, I. Buvat, G.J.R. Cook, C. Davatzikos, A. Depeursinge, M.C. Desseroit, N. Dinapoli, C.V. Dinh, S. Echegaray, I. El Naqa, A.Y. Fedorov, R. Gatta, R.J. Gillies, V. Goh, M. Götz, M. Guckenberger, S.M. Ha, M. Hatt, F. Isensee, P. Lambin, S. Leger, R.T. H. Leijenaar, J. Lenkowicz, F. Lippert, A. Losnegård, K.H. Maier-Hein, O. Morin, H. Müller, S. Napel, C. Nioche, F. Orlhac, S. Pati, E.A.G. Pfaehler, A. Rahmim, A.U. K. Rao, J. Scherer, M.M. Siddique, N.M. Sijtsema, J. Socarras Fernandez, E. Spezi, R. Steenbakkers, S. Tanadini-Lang, D. Thorwarth, E.G.C. Troost, T. Upadhaya, V. Valentini, L.V. van Dijk, J. van Griethuysen, F.H.P. van Velden, P. Whybra, C. Richter, S. Löck, The image biomarker standardization initiative: standardized quantitative radiomics for high-throughput image-based phenotyping, Radiology 295 (2020) 328–338.

[49] J.J.M. van Griethuysen, A. Fedorov, C. Parmar, A. Hosny, N. Aucoin, V. Narayan, R.G.H. Beets-Tan, J.C. Fillion-Robin, S. Pieper, H. Aerts, Computational radiomics system to decode the radiographic phenotype, Canc. Res. 77 (2017) e104–e107.

[50] H. Peng, F. Long, C. Ding, Feature selection based on mutual information criteria of max-dependency, max-relevance, and min-redundancy, IEEE Trans. Pattern Anal. Mach. Intell. 27 (2005) 1226–1238.

[51] T. Chen, C. Guestrin, Xgboost: a scalable tree boosting system, in: Proceedings of the 22nd Acm Sigkdd International Conference on Knowledge Discovery and Data Mining, 2016, pp. 785–794.

[52] S.H. Chen, Q.S. Wan, D. Zhou, T. Wang, J. Hu, Y.T. He, H.L. Yuan, Y.Q. Wang, K. H. Zhang, A simple-to-use nomogram for predicting the survival of early hepatocellular carcinoma patients, Front. oncol. 9 (2019) 584.

[53] J. Liu, Z. Liu, W. Jiang, J. Wang, M. Zhu, J. Song, X. Wang, Y. Su, G. Xiang, M. Ye, J. Li, Y. Zhang, Q. Shen, Z. Li, D. Yao, Y. Song, K. Yu, Z. Luo, L. Ye, Clinical predictors of COVID-19 disease progression and death: analysis of 214 hospitalised patients from Wuhan, China, Clin. Res. J (2020). In press.

[54] A. Izcovich, M.A. Ragusa, F. Tortosa, M.A. Lavena Marzio, C. Agnoletti, A. Bengolea, A. Ceirano, F. Espinosa, E. Saavedra, V. Sanguine, A. Tassara, C. Cid, H.N. Catalano, A. Agarwal, F. Foroutan, G. Rada, Prognostic factors for severity and mortality in patients infected with COVID-19: a systematic review, PloS One 15 (2020), e0241955.

[55] Q. Yang, X. Yang, Incidence and risk factors of kidney impairment on patients with COVID-19: a meta-analysis of 10180 patients, PloS One 15 (2020), e0241953.

[56] D. Colombi, F.C. Bodini, M. Petrini, G. Maffi, N. Morelli, G. Milanese, M. Silva, N. Sverzellati, E. Michieletti, Well-aerated lung on admitting chest CT to predict adverse outcome in COVID-19 pneumonia, Radiology 296 (2020) E86–E96.

[57] F. Zeng, L. Li, J. Zeng, Y. Deng, H. Huang, B. Chen, G. Deng, Can we predict the severity of coronavirus disease 2019 with a routine blood test? Pol. Arch. Intern. Med. 130 (2020) 400–406.

[58] H.B. Tan, F. Xiong, Y.L. Jiang, W.C. Huang, Y. Wang, H.H. Li, T. You, T.T. Fu, R. Lu, B.W. Peng, The study of automatic machine learning base on radiomics of non-focus area in the first chest CT of different clinical types of COVID-19 pneumonia, Sci. Rep. 10 (2020) 18926.

[59] I. Shiri, H. Maleki, G. Hajianfar, H. Abdollahi, S. Ashrafinia, M.G. Oghli, M. Hatt, M. Oveisi, A. Rahmim, PET/CT radiomic sequencer for prediction of EGFR and KRAS mutation status in NSCLC patients, in: IEEE Nuclear Science Symposium and Medical Imaging Conference Proceedings (NSS/MIC), IEEE, 2018, pp. 1–4.

[60] C. Parmar, P. Grossmann, J. Bussink, P. Lambin, H.J. Aerts, Machine learning methods for quantitative radiomic biomarkers, Sci. Rep. 5 (2015) 13087.

[61] L. Li, L. Qin, Z. Xu, Y. Yin, X. Wang, B. Kong, J. Bai, Y. Lu, Z. Fang, Q. Song, Artificial intelligence distinguishes COVID-19 from community acquired pneumonia on chest CT, Radiology (2020) 200905.

[62] A.J. DeGrave, J.D. Janizek, S.-I. Lee, AI for Radiographic COVID-19 Detection Selects Shortcuts over Signal, medRxiv, 2020.

[63] R.J. Gillies, P.E. Kinahan, H. Hricak, Radiomics: images are more than pictures, they are data, Radiology 278 (2016) 563–577.

[64] P. Lambin, R.T. Leijenaar, T.M. Deist, J. Peerlings, E.E. De Jong, J. Van Timmeren, S. Sanduleanu, R.T. Larue, A.J. Even, A. Jochems, Radiomics: the bridge between medical imaging and personalized medicine, Nat. Rev. Clin. Oncol. 14 (2017) 749–762.

[65] I. Shiri, H. Maleki, G. Hajianfar, H. Abdollahi, S. Ashrafinia, M. Hatt, H. Zaidi, M. Oveisi, A. Rahmim, Next-generation radiogenomics sequencing for prediction of EGFR and KRAS mutation status in NSCLC patients using multimodal imaging and machine learning algorithms, Mol. Imag. Biol. 22 (2020) 1132–1148.

[66] G. Hajianfar, I. Shiri, H. Maleki, N. Oveisi, A. Haghparast, H. Abdollahi, M. Oveisi, Noninvasive O6 methylguanine-DNA methyltransferase status prediction in glioblastoma multiforme cancer using magnetic resonance imaging radiomics features: univariate and multivariate radiogenomics analysis, World Neurosurgery 132 (2019) e140–e161.